Influence of structure dimensions on self-breathing micro fuel cells

S. Wagner [a,*], S. Krumbholz [b], R. Hahn [a], H. Reichl [b]

[a] *Fraunhofer Institute for Reliability and Microintegration, Berlin 13355, Germany*
[b] *Technische Universität Berlin, Center of Microperipherics, Berlin 13355, Germany*

ARTICLE INFO

ABSTRACT

In this paper a proton exchange membrane micro fuel cell (PEMFC) with a passive air breathing cathode and microstructured flow fields is studied comprehensively using a numerical model and experimental characterization. The design of the flow field structures is directly dependent on the fabrication technology. An optimization of structure dimensions is possible within the design space. A model is presented, which describes the influence of the aspect ratio of the channel width and the rib width of the micro flow field for a structure were no gas diffusion layers are incorporated. The fuel cell performance is limited by electrical losses in the electrode layer for large channel widths and by reactant transport for small channel widths.

© 2008 Elsevier B.V. All rights reserved.

1. Introduction

Recently a number of papers have been published dealing with the development of MEMS-based fuel cells [1–6]. There are two reasons for this development:

1. Using new technologies and designs it should be possible to significantly improve fuel cell performance when micro-scale phenomena are exploited. However, such benefits can only be realized if the fuel cell devices can be fabricated using available manufacturing techniques. They are in most cases adapted from semiconductor and microsystems technology. Fuel cells built to exploit micro-scale phenomena would be smaller, make better use of volume and could obtain improved heat and mass transfer. Technologies which may have the potential to solve problems which are critical in the conventional stack technology for example are
   - fabrication of micro-porous membranes optimized for two phase transport,
   - plasma polymerization of ion conducting polymers,
   - altering of hydrophilic, hydrophobic properties by plasma treatment, and
   - fabrication of transport optimized microflow fields with varying dimensions.

2. The majority of research on micro-scale fuel cells is also aimed at micro-power applications. There are many new miniaturized applications which can only be realized if a higher energy density power source is available compared to button cells and other small batteries. Miniaturization down to these dimensions is not possible with conventional fuel cell stack technology.

Most of the approaches for MEMS fuel cells comprise basic research and material development. What these approaches have in common is that they require great effort to establish the process and to optimize the electro-kinetic performance of the catalyst layer.

Today, the production of fuel cells is linked with high manufacturing costs. Crucial for the successful design of fuel cells is an understanding of how the design and manufacturing processes influence performance. In our approach no gas diffusion layers (GDLs) are used in order to achieve a simple fabrication technology. However, a GDL-less design results in higher transverse losses between the flow field ribs in the catalyst layer.

This paper presents a model for the theoretical study of a planar self-breathing proton exchange membrane micro fuel cell (PEMFC) with microstructured flow fields used in the anodic and cathodic current collectors.

Printed circuit board (PCB) technologies like wet etching and galvanic deposition are investigated for the micropatterning of flow field structures in order to evaluate the limits of these technologies. Based on the modelling results and measurements an optimized flow field design can be realized which builds the bridge between best fuel cell performance and low cost fabrication technology

* Corresponding author. Present address: Fraunhofer IZM, Gustav-Meyer-Allee 25, Berlin 13355, Germany. Tel.: +49 30 46403 609; fax: +49 30 46403 123.
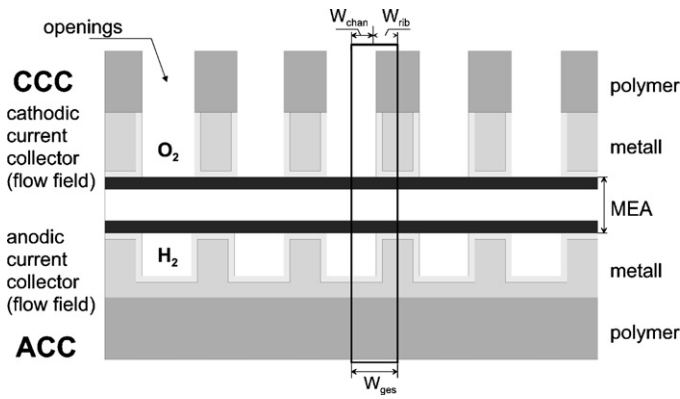*E-mail address:* stefan.wagner@izm.fraunhofer.de (S. Wagner).

Fig. 1. Schematic cross-section of a self-breathing micro-PEMFC.

for the current collectors with integrated, microstructured flow fields.

2. Design concept of the microfuel cell

A planar design allows a passive, fully self-breathing operation of the fuel cell. Additional fans or air pumps are not needed. In order to achieve higher voltages, pluralities of cells have to be connected in serial, where the cathode is connected to the anode of the following cell.

For low cost assembly it is necessary that the fuel cells are constructed without additional GDLs. A continuous piece of GDL results in a short circuit between adjacent cells. To avoid this, a separate GDL for each single cell must to be assembled. This is contrary to the idea of processing thousands of fuel cells at the same time using wafer and foil processing. Therefore, diffusion layers are not used in this design concept [5].

The microstructures fabricated on the inner sides of the current collectors are in the dimension range of carbon fibers in conventional diffusion layers. Moreover, the microstructures serve as the flow field and are designed to assure a homogenous gas supply all over the membrane electrode assembly (MEA).

This way the complete fuel cell consists only of three foils: the current collector foils with integrated flow fields on top and bottom and the patterned MEA foil in-between. Fig. 1 shows a cross-sectional view of the microfuel cell.

3. Model

3.1. Model approach

The numerical model presented here is a two-dimensional, isothermal, stationary model of a complete planar self-breathing PEMFC including current collectors, flow field, and MEA. Fig. 1 shows a schematic cross-section of the studied micro-PEMFC. The electrochemical reactions are described by the Tafel equation. The potential and current balance equations are solved separately for the protons and electrons. The charge transport of electrons and protons is described by a charge balance equation in combination with Ohm's law. The mass transport of the gaseous species (H_2, O_2, H_2O, N_2) in the electrodes and channel zones is described using the Maxwell–Stefan equation. The source and sink terms of the gaseous species are linked to the electrochemical reaction rates which are located in the catalyst layers.

The produced water is assumed to be generated in the gaseous phase. The water transport across the membrane is described using a concentrated solution approach. The phase change of water is
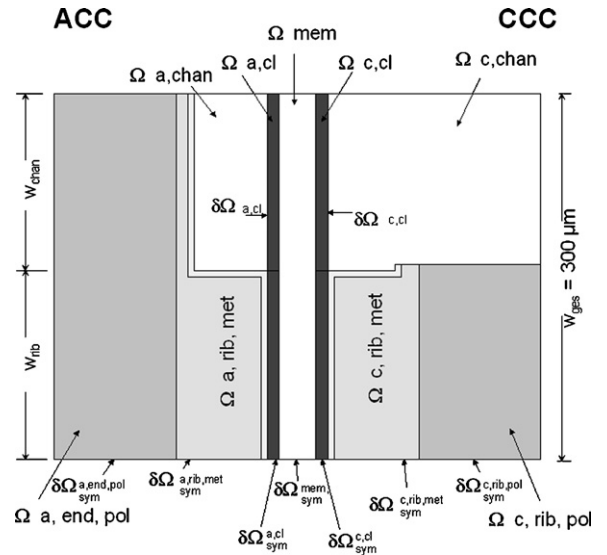

Fig. 2. Schematic illustration of the modeled symmetry element.

neglected. Heat transport is not taken into account in this model. Hydrogen gas flow in the anode flow field is not taken into account due to the high stoichiometric ratios in the experiment and fast anode kinetics. Therefore, only gaseous diffusion is assumed to limit the supply of hydrogen at the anodic electrode.

3.2. Model geometry

The two-dimensional model geometry, which was used, represents a symmetry element of the real geometry which has to be thought of as being a repeating part of the real cell geometry in Fig. 1. Fig. 2 shows a schematic drawing of the modeled symmetry element of the fuel cell. Domains are marked with Ω and boundaries with $\delta\Omega$. Anode (ACC) and cathode (CCC) are on left and right side, respectively. Table 1 gives an overview of the dimensions of the fuel cell which was simulated.

3.3. Governing differential equations

The mass balance is taken into account on the cathode and on the anode by the divergence of the diffusive mass flux. This diffusive mass flux is described using the Maxwell–Stefan equation set up on a mass basis [8,9] (Table 2)

$$\nabla \cdot \left[-\rho_{c,a} w_i \sum_{j=1}^{N} D_{ij} \left(\frac{M_{c,a}}{M_j} \right) \left(\nabla w_j + w_j \left(\frac{\nabla M_{c,a}}{M_{c,a}} \right) \right) \right] = Q_i^M \quad (1)$$

Table 1
Dimension of the subdomains used in the simulation

Subdomain	Name	Dimension (μm)
$\Omega_{a,end,pol}$, $\Omega_{c,end,pol}$	Anode/cathode endplate (polymer)	100
$\Omega_{a,rib,met}$, $\Omega_{c,rib,met}$	Anode/cathode metal layer	70
Ω_{mem}	Membrane	25
$\Omega_{a,cl}$, $\Omega_{c,cl}$	Anode/cathode catalytic layer	10
$\Omega_{a,chan}$	Anode channel	
	Depth	60
	Width	100–500
$\Omega_{c,chan}$	Cathode opening width	100–300

Table 2
Nomenclature

Symbol	Dimension	Denotation
$j_{0,a}$	$A\,m^{-2}$	Anodic exchange current density
α_a	–	Anodic symmetry coefficient
$j_{0,c}$	$A\,m^{-2}$	Cathodic exchange current density
α_c	–	Cathodic symmetry coefficient
σ	$\Omega^{-1}\,m^{-1}$	Conductivity
q	$C\,m^{-3}\,s^{-1}$	Source of charge
Φ_e	V	Potential of the electronic conductive phase
Φ_p	V	Potential of the ionic conductive phase
$\Delta\Phi_a^{ref}$	V	Anodic Galvani potential
$\Delta\Phi_c^{ref}$	V	Cathodic Galvani potential
V_{cell}	V	Cell voltage
F	$C\,mol^{-1}$	Faraday constant
R	$J\,mol^{-1}\,K^{-1}$	Universal gas constant
P	Pa	Pressure
T	K	Temperature
$M_{c,a}$	$kg\,mol^{-1}$	Molar mass of gas mixture on cathode and anode side
Q^M	$kg\,m^{-3}\,s^{-1}$	Mass source term
$\rho_{c,a}$	$kg\,m^{-3}$	Density of gas mixture on cathode and anode side
ω_I	–	Mass fraction of species i
x_i	–	Molar fraction of species i

The density of the gas mixture on the cathode side is given by

$$\rho_c = M_c \frac{P^{ref}}{RT} \tag{2}$$

with

$$M_c = M_{O_2} x_{O_2} + M_{N_2} x_{N_2} + M_{H_2O} x_{H_2O} \tag{3}$$

and for the anode side

$$\rho_a = M_a \frac{P^{ref}}{RT} \tag{4}$$

with

$$M_a = M_{H_2} x_{H_2} + M_{H_2O} x_{H_2O} \tag{5}$$

The charge transport of electrons (l = e) and protons (l = p) is governed by a charge balance in combination with Ohm's law:

$$\nabla \cdot j_l = q_l \tag{6}$$

$$j_l = -\sigma_l \nabla \Phi_l \tag{7}$$

Here j_l, q_l and σ_l denote the current density, the source terms for the current, and the conductivities for electrons and ions, respectively.
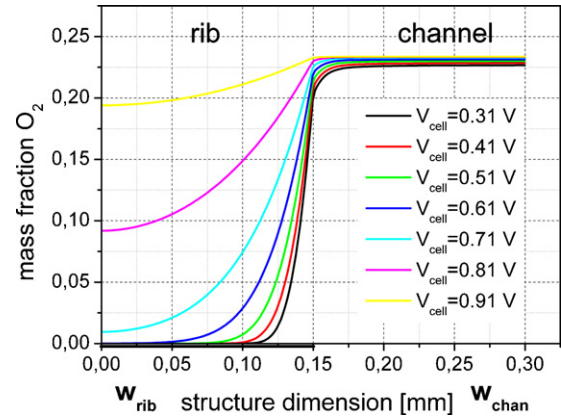
3.4. Source terms

Sources and sinks for the current are located in the catalytic layer ($\Omega_{a,cl}$, $\Omega_{c,cl}$). The kinetics of the electrochemical reactions are approximated by the Tafel approach [7]

$$q_c = a\, j_{0,c} \left(\frac{x_{O_2}}{x_{O_2}^{ref}} \right) \exp\left(-\left(\frac{2\alpha_c F}{RT} \right) (\Phi_e - \Phi_p - \Delta\Phi_c^{ref}) \right) \tag{8}$$

$$q_a = a\, j_{0,a} \left(\frac{x_{H_2}}{x_{H_2}^{ref}} \right) \exp\left(\left(\frac{2(1-\alpha_a)F}{RT} \right) (\Phi_e - \Phi_p - \Delta\Phi_a^{ref}) \right) \tag{9}$$

a indicates the active surface of the Pt-catalyst per volume, $j_{0,c}$ and $j_{0,a}$ are the exchange current densities of the oxygen reduction reaction in the cathode and the hydrogen oxidation reaction in the anode at reference conditions. $\Delta\Phi_{c,a}^{ref}$ describes the potential difference between the electrode and membrane phases at equilibrium conditions and Φ_p and Φ_e denote the potential of proton-conducting and of the electric-conducting phase, respectively.

Fig. 3. Profiles of the oxygen distribution within the catalyst layer for cell voltages V_{cell} in between 0.31 and 0.91 V.

The source terms of the potential Eq. (6) are

$$q_e = \begin{cases} -q_a & \text{in } \Omega_{a,cl} \\ q_c & \text{in } \Omega_{c,cl} \end{cases} \tag{10}$$

$$q_p = \begin{cases} q_a & \text{in } \Omega_{a,cl} \\ -q_c & \text{in } \Omega_{c,cl} \end{cases}. \tag{11}$$

4. Simulation results

To analyse the impact of the dimensions of the flow field designs on the electrical properties of the fuel cell without GDL, flow field structures with dimensions in between 100 and 500 μm were examined in the simulation.

Fig. 3 shows the profiles of the oxygen distribution in the cathodic catalyst layer at the boundary to the membrane in the domain of the channel (w_{chan}) and the rib (w_{rib}) for different cell voltages between 0.31 and 0.91 V. The size of the rib is indicated by the black mark on the x-axis. Due to the use of the symmetry element the values on the x-axis only depict half of the channel and rib widths w_{chan} and w_{rib}. The oxygen mass fraction within the area of a rib is strongly decreasing for smaller cell voltages and therewith higher current densities such that there is no oxygen left for the cathodic reaction.

Fig. 4 illustrates the distribution of the protonic current density within the membrane and the anodic and cathodic catalyst layers at a cell voltage of 0.61 V. At the boundary of the cathodic current collector to the channel a local maximum of the current density is visible.

The profiles of the protonic current density within the cathodic catalyst layer at the boundary of the membrane for different cell voltages are depicted in Fig. 5. A significantly inhomogeneous distribution of the protonic current density can be seen for lower voltages. Underneath the current collector ribs (w_{rib}) the current density approaches zero.

Due to the higher oxygen concentration the protonic current densities are bigger within the channel. At the transition between the channel and the rib a maximum can be observed, which is stronger for lower cell voltages. Although a sufficient concentration of hydrogen is provided underneath the rib on the anode side, the protonic current densities on the anode side are decreasing as well. Depending on the protonic conductivity, the protons can only bypass the covered area on the cathode side in a limited way to react with oxygen. Hence the protonic current density on the cathode side is decreasing due to the limited supply of oxygen.
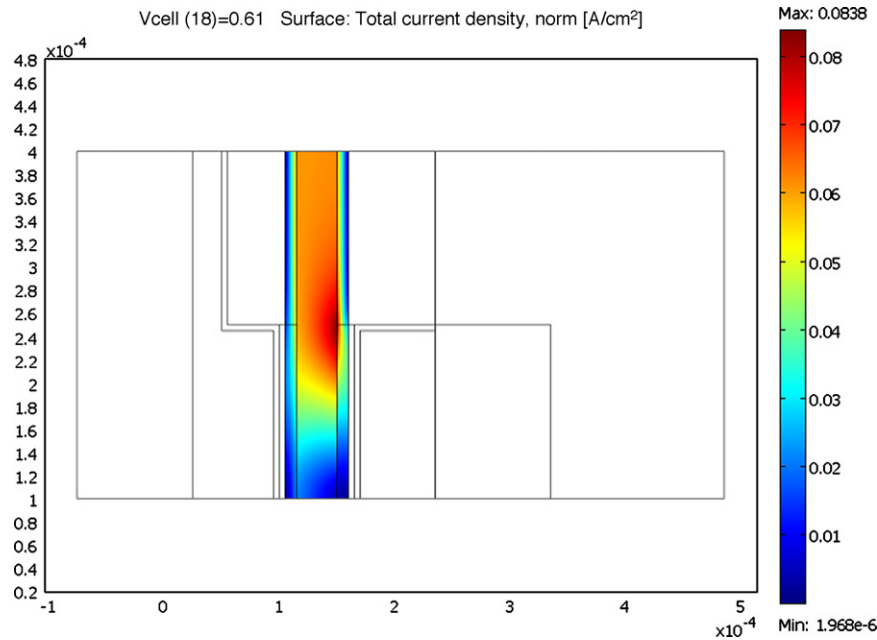
Fig. 4. Illustration of the protonic current distribution within the membrane and catalyst layers for a cell voltage of 0.61 V.

The distribution of the electrical current density within the catalyst layers and the current collectors at a cell voltage of 0.61 V is illustrated in Fig. 6.

The profile of the electrical current density within the catalyst layer on the anode side at a cell voltage of 0.61 V is shown in Fig. 7. The different widths of the current collector ribs are marked on the x-axis.

The widths of the current collectors on the anode side $w_{\text{rib\_an}}$ were varied, the dimensions on the cathode side were kept constant. The current density underneath the rib (close to the edge) is not decreasing to zero, as it seems in Fig. 7. There are just comparatively small current densities in this area, which are superposed in this diagram. The biggest part of the current density is within the area of the channel. Because of the lateral conduction the local current density within the channel is increasing towards the current collector and is distributed in the catalyst layer underneath the rib. For a rib width $w_{\text{rib\_an}} = 500\,\mu\text{m}$ a maximum can be seen within the rib area. The current density underneath the rib is increasing and reaches a maximum at 150 μm.

This can be attributed to the dimensions of the structures on the cathode side. Considering the symmetry element for the chosen rib widths of 300 μm, the rib area starts at 150 μm.

4.1. Effect of the anodic flow field structure

To examine the impact of the current collector on the performance of the fuel cells in a wider operating range in more detail, current–voltage–relations in between 0.95 and 0.25 V were calculated with the help of the model and depicted as current–voltage-diagrams. In the following the dependence of fuel cell performance on the anodic current collector is examined. For this purpose the widths of the ribs ($w_{\text{rib\_an}}$) were varied in the model and the respective current–voltage-diagrams needed to be calculated. The widths used in the model were between 50 and 250 μm with a constant pitch of 300 μm. Due to the use of the symmetry element these would correspond to actual widths between 100 and 500 μm with a pitch of 600 μm. A constant pitch causes the width of the channel ($w_{\text{chan\_an}}$) to be reduced with increasing rib width and thus leads to a smaller reactive area. The dimensions on the cathode side were kept constant under these circumstances.

As observed for the mass fraction distribution, an increased sheet resistance resulted from the larger spacing of current collectors with a smaller width, and is the more limiting factor. The area of the cathodic catalyst that is covered by the current collector has a much smaller negative impact. With a power density of ca. 112 mW cm^{-2} a power maximum can be observed for the fuel cell with the widest anodic current collector ($w_{\text{rib\_an}} = 500\,\mu\text{m}$). In contrast to this the maximal power of the fuel cell with the smallest anodic current collector ($w_{\text{rib\_an}} = 100\,\mu\text{m}$) is only 59 mW cm^{-2}.

The calculated power densities for the maxima of the different anodic rib widths ($w_{\text{rib\_an}}$) are illustrated in Fig. 8. It can be noticed that the gain in power density is decreasing with an increasing width of the ribs of the anodic flow field ($w_{\text{rib\_an}}$). The limiting factor for lateral conductivity within the cathodic catalyst that constrains the power density of the fuel cell decreases with decreasing channel width due to the lateral conduction.
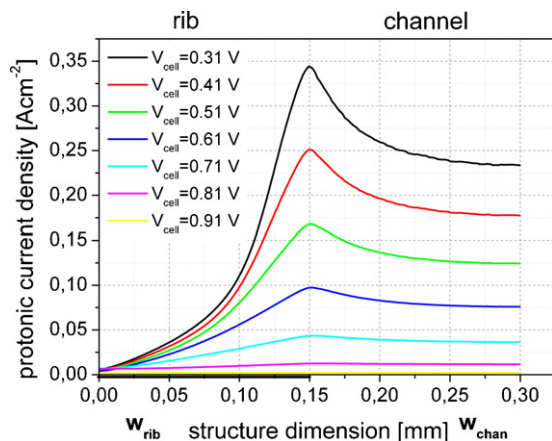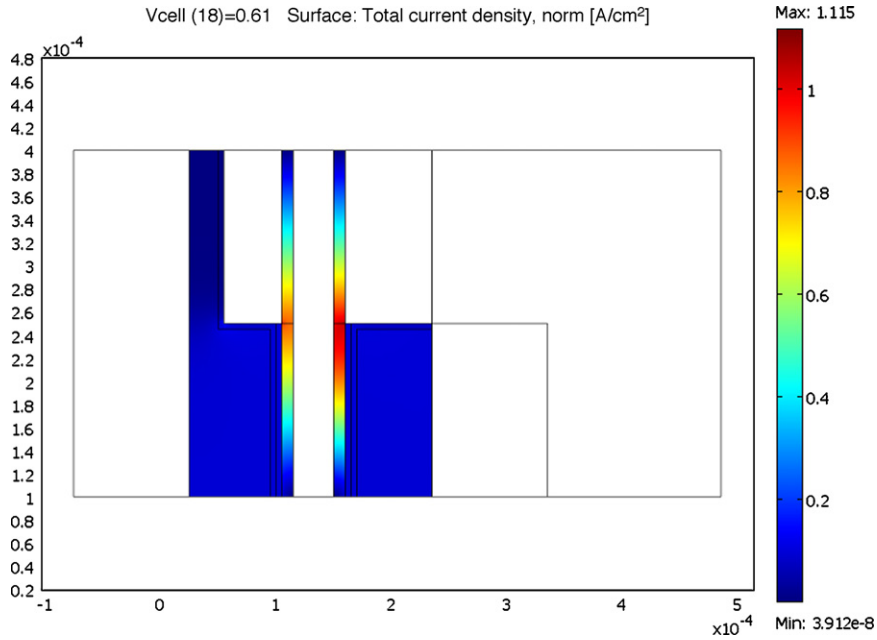

Fig. 5. Profiles of the protonic current density within the catalyst layer for the cell voltage V_{cell} in between 0.31 and 0.91 V.

Fig. 6. Illustration of the electrical current distribution within the catalyst layer and the current collectors for a cell voltage of 0.61 V (anodic current collector on the left, cathodic current collector on the right).
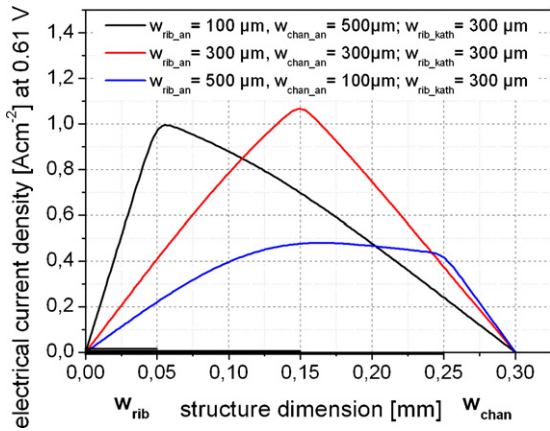

Fig. 7. Profile of the electric current density within the anodic catalyst layer at the boundary to the electrolyte for a cell voltage $V_{cell} = 0.61$ V for different rib widths w_{rib_an} of 100, 300, and 500 μm on the anode side and a constant rib width w_{rib_kath} of 300 μm on the cathode side.

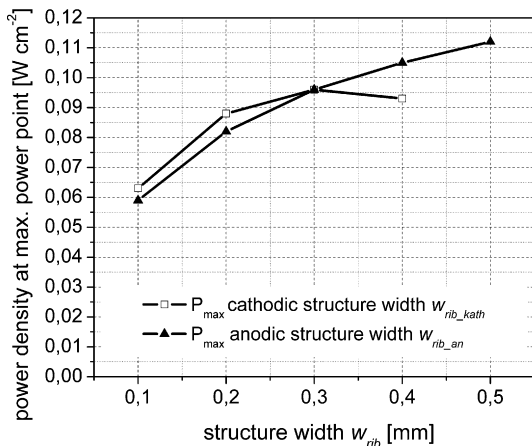### 4.2. Effect of the cathodic flow field structure

To examine the impact of the cathodic current collector on the performance of the fuel cell current–voltage diagrams were calculated for different cathodic current collector dimensions. For this model variation the anodic dimensions, openings for the air supply in the polymer structure on the cathode side, and the pitch p were kept constant.

It can be seen that the cathodic current collector (w_{rib_kath}) has a significant effect on the maximum power densities of fuel cells. The impact of the lateral conductivity and the limitation due to transverse losses for a big channel width (w_{chan_kath}), respectively is superposed by losses due to supply limitations for decreasing w_{chan_kath}.

From Fig. 8 one can notice that a pronounced optimum exists for a channel to rib width ratio of 1:1. A pitch of $p = 600$ μm corresponds to a rib width $w_{rib\_kath} = 300$ μm. The diagram in Fig. 9 illustrates the power density at the power maximum dependent on the rib width of the cathodic current collector with a constant air opening
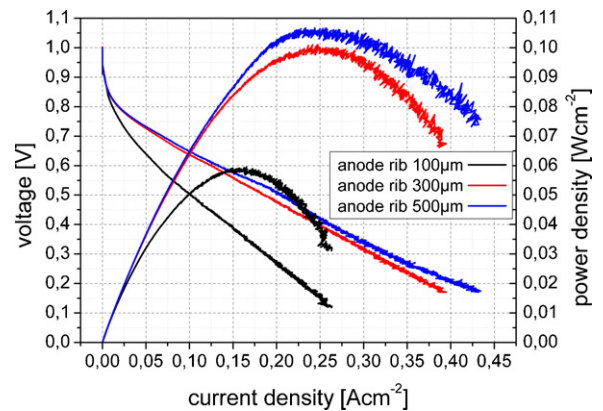

Fig. 8. Calculated power density for the power maximum depending on the anodic and cathodic structure width w_{rib_an}.

Fig. 9. Electrical characterisation ($T = 25$ °C, rF = 25%) of planar cells with constant values for the cathodic structures ($w_{rib\_kath} = 300$ μm) and variation of the anodic structures.

width and geometry on the anode side. In this case the maximum power density of approximately 96 mW cm^{-2} is achieved for equal rib and channel widths width of 300 μm.

5. Electrical characterization of single cells as function of flow field structure

Prototypes of self-breathing PEM fuel cells with a size of 1 cm × 2 cm and 400 μm thickness were realized in order to compare the measurement and modeling results [5,6,10].

The prototypes are fabricated by using PCB technology. Based on 100 μm FR4 substrates a laminated Cu-layer with a thickness of 70 μm is patterned by wet etching. Long-term stability of the metal layer is achieved by using an Au protection layer. The openings for the hydrogen in- and outlet and for the openings on the cathode side are realized by LASER cutting.

In analogy to the simulation different anodic flow field designs are realized. Based on a constant pitch of 600 μm the rib width of the flow field structure is varied from 100 to 500 μm.

Fig. 9 shows the measured polarization curves and the power density as a function of the current density for three different designs of the anodic flow field. The cathodic flow field structure and the size of the opening are constant for all cells. A maximal power density of 105 mW cm^{-2} could be achieved with a channel width of 100 μm and a rib width of 500 μm.

All measurements are carried out at room temperature with a constant dry hydrogen supply and natural convection on the cathode side.

5.1. Validation

The validation of the model is performed by comparing the measured polarization curves of the different fuel cells with the simulated variation of the anodic flow field design. The polarization curves resulting from the simulation for the corresponding geometric variation together with the experimentally measured results are depicted in Figs. 10 and 11.

The model results show a good correlation with the measured polarization curves. The differences between the various anodic flow field geometries are substantial for small flow field ribs. For increasing channel width the electrical transverse losses dominate. The transport limitations of the hydrogen for decreasing channel width have a marginal effect on the fuel cell performance.
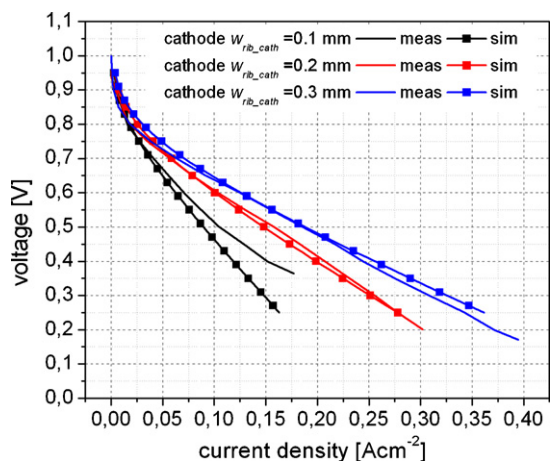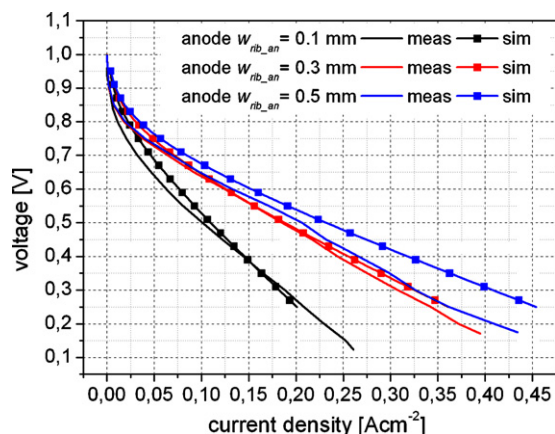
Fig. 11. Comparison of simulation and measurement ($T = 25$ °C, rF = 25%) with constant values for the cathodic structures ($w_{rib\_kath} = 300$ μm) and variation of the anodic structures.

6. Summary

A simplified, two-dimensional, isothermal, steady-state numerical model for the simulation of planar self-breathing PEM fuel cells without gas diffusion layers has been developed. Simulations were carried out for a variety of anodic flow field geometries. Significant limitations due to lateral electrical losses were observed in the simulated polarization curves. For increasing channel width of the anodic flow field structure the electrical lateral losses due to the low electrical conductivity of the catalytic layer dominate the fuel cell performance. The model-based optimization of the flow field structures has shown, that rib widths <50 μm are necessary for the cathodic current collectors in order to keep the decrease in oxygen mass fraction low underneath the rib. However, big channel widths lead to increased electrical losses. Through simulation it was determined that an optimal operation of a fuel cell with a pitch of 600 μm is given for equal channel and rib widths.

On the anode side the electrical losses have a bigger impact on the performance than the mass fractions. Even for a rib width of 500 μm hydrogen is supplied sufficiently to the catalyst layer underneath the ribs. Small channels and wide structures for the current collectors lead to the smallest electrical losses and thereby highest power densities.

The characteristics generated with the numerical model are all based on the same set of parameters, which were taken from literature.

The numerical model was verified with measurements of PEM fuel cells with varying structure dimensions. Excellent agreement was achieved between measurement and simulation.

The presented numerical model gives a better understanding of the impact of the anodic flow field structure of micro-PEMFCs without gas diffusion layers. This design of a PEM microfuel cell is very interesting for low-cost mass production based on printed circuit board technologies [11]. The results are well suited to optimize the microfuel cell flow field design of a given fabrication technology.

Fig. 10. Comparison of simulation and measurement ($T = 25$ °C, rF = 25%) with variation of the cathodic structures and constant values for the anodic structure ($w_{rib\_an} = 300$ μm, $p = 600$ μm).

References

[1] K.B. Min, S. Tanaka, M. Esashi, J. Micromech. Microeng. 16 (2006) 505–511.
[2] L. Mex, J. Müller, Membr. Technol. 115 (1999) 5–9.
[3] J.P. Meyers, H.L. Maynard, J. Power Sources 109 (2002) 76–88.
[4] T. Pichonat, B. Gauthier-Manuel, J. Micromech. Microeng. 15 (2005) 179–184.
[5] R. Hahn, S. Wagner, A. Schmitz, H. Reichl, J. Power Sources 131 (2004) 73–78.
[6] A. Schmitz, M. Tranitz, S. Wagner, R. Hahn, C. Hebling, J. Power Sources 5213 (2003) 1–10.
[7] C.H. Hamann, W. Vielstich, Electrochemistry, Wiley-VCH, Weinheim, 1998.

[8] C. Ziegler, A. Schmitz, M. Tranitz, E. Fontes, J.O. Schumacher, J. Electrochem. Soc. 151 (2004) 2028–2041.

[9] A. Schmitz, C. Ziegler, J.O. Schumacher, M. Tranitz, E. Fontes, C. Hebling, Fuel Cells, vol. 4 (4), Wiley-VCH, Weinheim, 2004.

[10] S. Wagner, R. Hahn, T. Fischer, F. Ebling, H. Reichl, M. Krumm, K. Marquardt, Micro System Technol. (2003) 303–311.

[11] S. Wagner, R. Hahn, H.P. Monser, R. God, mst-news 04/2005, VDI/VDE-IT, 2005, pp. 34–36.